Linking Overturning, Recirculation, and Melt in Glacial Fjords

Ken Zhao[1], Andrew Stewart[2], and James C. McWilliams[2]

[1]UCLA
[2]University of California Los Angeles

November 22, 2022

Abstract

Fjord circulation modulates the connection between marine-terminating glaciers and the ocean currents offshore. These fjords exhibit both overturning and horizontal recirculations, which are driven by water mass transformation at the head of the fjord via subglacial discharge plumes and distributed meltwater plumes. However, little is known about the interaction between the 3D fjord circulation and glacial melt and how relevant fjord properties influence them. In this study, high-resolution numerical simulations of idealized glacial fjords demonstrate that recirculation strength controls melt, which feeds back on overturning and recirculation. The overturning circulation strength is well predicted by existed plume models for face-wide melt and subglacial discharge, while relationships between the overturning, recirculation, and melt rate are well predicted by vorticity balance, reduced-order melt parameterizations, and empirical scaling arguments. These theories allow improved predictions of fjord overturning, recirculation, and glacial melt by taking intrafjord dynamics into account.

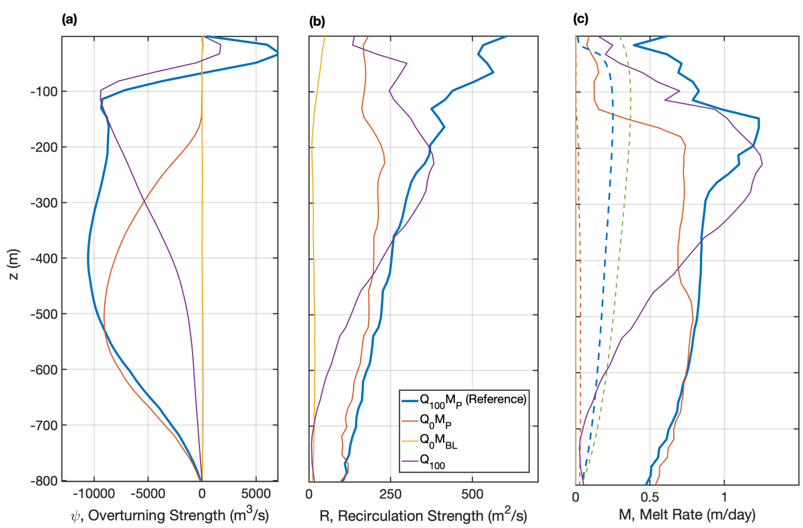

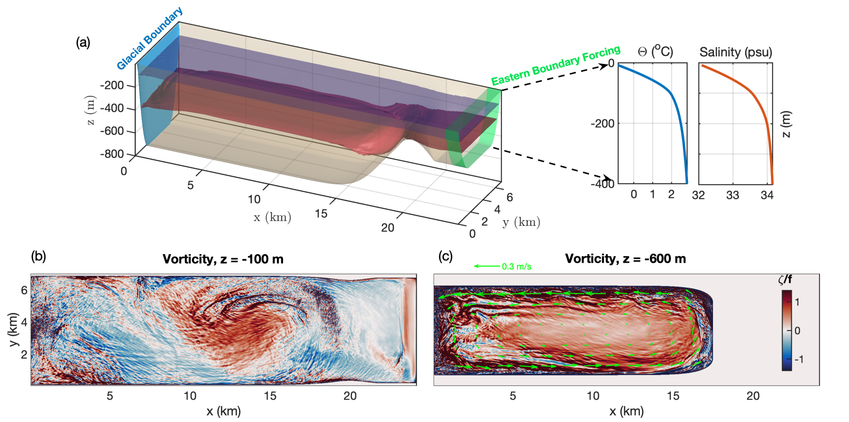

(a)
Glacial Boundary
Eastern Boundary Forcing
z (m)
x (km)
y (km)
Θ (°C)
Salinity (psu)
z (m)
(b)
Vorticity, z = -100 m
y (km)
x (km)
(c)
Vorticity, z = -600 m
0.3 m/s
ζ/f
x (km)

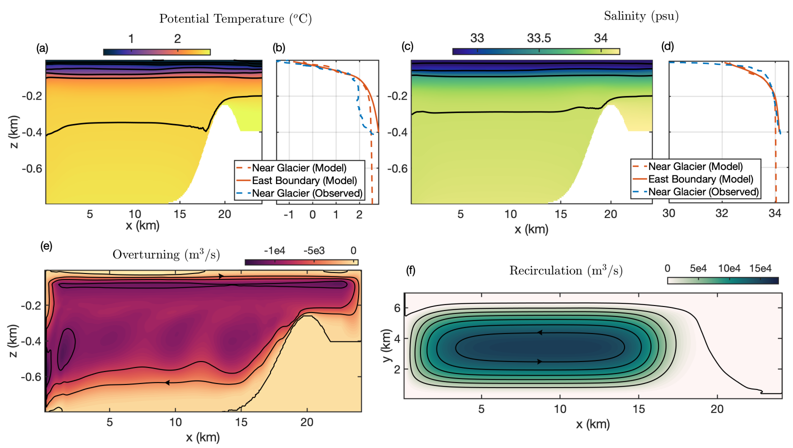

Potential Temperature (°C)
(a)
(b)
z (km)
x (km)
Near Glacier (Model)
East Boundary (Model)
Near Glacier (Observed)
Salinity (psu)
(c)
(d)
Near Glacier (Model)
East Boundary (Model)
Near Glacier (Observed)
x (km)
(e)
Overturning (m^3/s)
z (km)
x (km)
(f)
Recirculation (m^3/s)
y (km)
x (km)

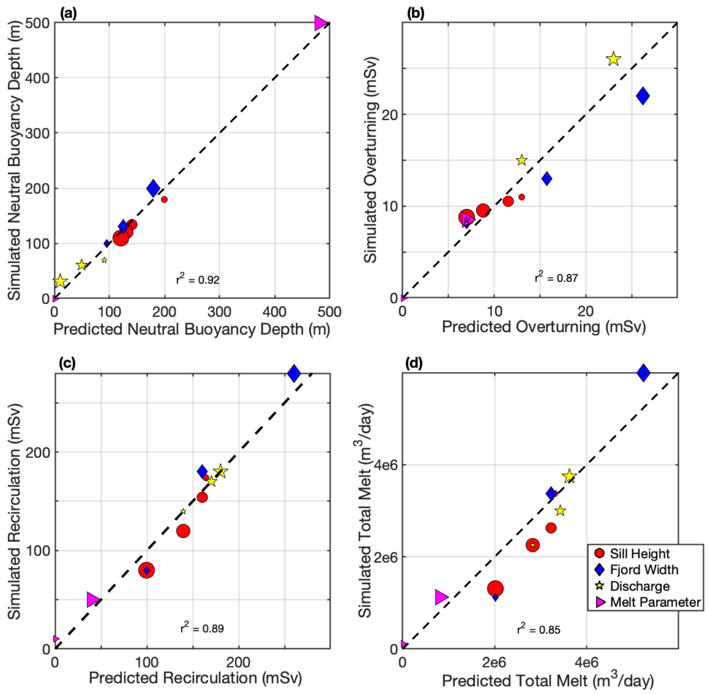
(a)
Simulated Neutral Buoyancy Depth (m)
Predicted Neutral Buoyancy Depth (m)
r2 = 0.92
(b)
Simulated Overturning (mSv)
Predicted Overturning (mSv)
r2 = 0.87
(c)
Simulated Recirculation (mSv)
Predicted Recirculation (mSv)
r2 = 0.89
(d)
Simulated Total Melt (m3/day)
Predicted Total Melt (m3/day)
r2 = 0.85
Sill Height
Fjord Width
Discharge
Melt Parameter

Linking Overturning, Recirculation, and Melt in Glacial Fjords

Ken X. Zhao[1], Andrew L. Stewart[1], and James C. McWilliams[1]

[1]Department of Atmospheric and Oceanic Sciences, University of California, Los Angeles, 405 Hilgard Ave., Los Angeles, CA 90095-1565.

Key Points:

- Simulations show face-wide glacial melt dominates the total melt due to its concentration at deeper depths vs. discharge plume-driven melt.
- Glacial melt in fjords is primarily driven by recirculation at depth for most fjord properties, which is in turn driven by overturning.
- Face-wide glacial melt drives a significant warm-water overturning and recirculation at depth, leading to a melt-circulation feedback.

Corresponding author: Ken X. Zhao, kzhao@atmos.ucla.edu

Abstract

Fjord circulation modulates the connection between marine-terminating glaciers and the ocean currents offshore. These fjords exhibit both overturning and horizontal recirculations, which are driven by water mass transformation at the head of the fjord via subglacial discharge plumes and distributed meltwater plumes. However, little is known about the interaction between the 3D fjord circulation and glacial melt and how relevant fjord properties influence them. In this study, high-resolution numerical simulations of idealized glacial fjords demonstrate that recirculation strength controls melt, which feeds back on overturning and recirculation. The overturning circulation strength is well predicted by existed plume models for face-wide melt and subglacial discharge, while relationships between the overturning, recirculation, and melt rate are well predicted by vorticity balance, reduced-order melt parameterizations, and empirical scaling arguments. These theories allow improved predictions of fjord overturning, recirculation, and glacial melt by taking intrafjord dynamics into account.

Plain Language Summary

Glacial fjords are long, narrow, and deep inlets that connect glaciers to the open ocean. These glacial fjords exist around the margins of Greenland, West Antarctica, Patagonia, Alaska, and other regions, and collectively contribute a significant source of ice discharge into the ocean. Over the past two decades, tidewater glaciers in Greenland have accelerated, which can lead to sea level rise, and there is growing evidence that this acceleration is caused by deep warm water currents that flow into the fjords from the open ocean. These warm water currents have the potential to melt the submarine sides of the tidewater glaciers, causing them to retreat over time. The dynamics of this delivery of warm water to the glacier face, particularly its interaction with fjord circulation, are presently poorly understood. In this study, we use high-resolution, process-oriented simulations to understand the currents within these fjords, how they vary with different fjord characteristics, and how they lead to different rates of submarine melting of the glacier face. We find that the submarine glacial melt can cause feedbacks by amplifying the strength of the ocean currents, which further increase glacial melt. These results are an important step towards understanding a critical process that may help us improve sea level rise predictions.

1 Introduction

Outflowing of marine-terminating glaciers at the margins of the Greenland Ice Sheet and Antarctic Ice Sheet has accelerated in recent years (van den Broeke et al., 2016). For the Greenland Ice Sheet, a major cause of the accelerated melting is postulated to be the warming of deep ocean currents that come into contact with the termini of tidewater glaciers (Wood et al., 2018; Cowton et al., 2018; P. R. Holland et al., 2008; Straneo & Heimbach, 2013).

Submarine melt at marine-terminating glaciers drives glacial retreat and also amplifies iceberg calving depending on the properties of the glacier and fjord (Slater et al., 2021; Wood et al., 2021; Morlighem et al., 2016; Chauché et al., 2014; Fried et al., 2018; Rignot et al., 2015; Wagner et al., 2016). The submarine melt rate consists of ambient face-wide melt and discharge plume-driven melt (Straneo & Cenedese, 2015; Jackson et al., 2019). Although subglacial discharge plumes have the potential to drive a melt rate of more than a meter per day in the glacial area near the plume (equivalent to a volumetric melt of $\mathcal{O}(10^4)$ to $\mathcal{O}(10^5)$ m^3/day, assuming a fjord width of 5 km), it only occupies a small fraction of the glacial face (Cowton et al., 2015; Slater et al., 2018). By comparison, face-wide melting occurs along the entire glacial face as a result of either convection (Magorrian & Wells, 2016) or fjord circulation (Bartholomaus et al., 2013). Estimates of face-wide melt rates range widely, but are generally below 1 meter per day (and may be up to $\mathcal{O}(10^6)$ m^3/day of volumetric melt, based on an average glacial face area). Yet, only recently have studies considered the possibility that existing parameterizations of the ice-ocean boundary layer may be underestimating the contribution of face-wide melt (Jackson et al., 2019; Slater et al., 2018).

Fjord circulation has primarily been studied in the context of an estuary-like overturning circulation where warm and salty open-ocean water masses flow into the fjords at depth, and colder and fresher water masses flow out of the fjord at shallower depths (Stigebrandt, 1981; Farmer & Freeland, 2021; Inall & Gillibrand, 2010; Cottier et al., 2010). However, compared to most estuaries (Geyer & MacCready, 2014), deep glacial fjords in Greenland have relatively weak tidal influence and most of the vertical mixing is posited to occur near the glacial face (Straneo & Cenedese, 2015). The focus of previous 2D and 3D simulations of the shelf-to-fjord system has been to understand the sensitivity of glacial melt and the overturning circulation/fjord renewal to various fjord characteristics and atmospheric/oceanic drivers (e.g., Gladish et al. (2015), Sciascia et al. (2013), Xu et al. (2012), and Jackson et al. (2018)).

So far there are very few process-oriented models or theoretical efforts to quantify the interaction between fjord circulation and glacial melt rate within fjords. Along with the relative scarcity of ocean observations near marine-terminating glaciers, only recently has the horizontal recirculation within fjords and their sensitivity to fjord and forcing parameters received attention in models (Zhao et al., 2019, 2021), which has been suggested to have an influence on the face-wide melt rates (Slater et al., 2018; Jackson et al., 2019; Zhao et al., 2021; Carroll et al., 2017). Existing melt parameterizations either do not take into account horizontal near-glacier velocities (e.g., Sciascia et al. (2013), Xu et al. (2012)) or do not resolve the horizontal flows necessary for accurate melt rate predictions (e.g., Cowton et al. (2015), Carroll et al. (2017)). To remedy this, bulk glacial melt parameterizations should ideally use either near-glacier horizontal velocities based on resolved circulations or use predictions of near-glacier horizontal velocities in terms of the fjord forcing, geometry, and stratification.

To better understand these processes, we conduct a process-oriented exploration of fjord parameter space using simulations that can finely resolve the near-glacier horizontal circulation. We support these simulations with simple dynamical theories of overturning circulation, horizontal recirculation in the fjord interior, and glacial melt rate. Using these results, we address a gap in understanding of how fjord circulation and glacial melt co-interact, which has important implications for glacial retreat at the oceanic margins of ice sheets.

2 Fjord Model Setup

2.1 Model Configuration

To examine the interaction of fjord circulation and glacial melt, we use the Massachusetts Institute of Technology general circulation model (MITgcm, Marshall et al. (1997)) in a series of idealized high-resolution simulations. Our model uses an idealized geometric representation of a simple bathtub-like fjord-only domain with sloping side walls, a glacier face along its western boundary, and a Gaussian zonal sill centered at x_S = 20 km (see Fig. 1a). The model domain dimensions are $L \times W \times H$ = 25 km $\times$ 6 km $\times$ 800 m. There is quadratic bottom drag with a coefficient of 2×10^{-3} and no surface forcing. The eastern boundary region is nudged to a prescribed open ocean stratification in our reference experiment, based on near-fjord mouth observations from Ilulissat Icefjord (Gladish et al., 2015; Straneo & Cenedese, 2015), and includes a barotropic tidal velocity boundary condition in two of our perturbation experiments. See supplemental materials S-1 for further information on the model setup.

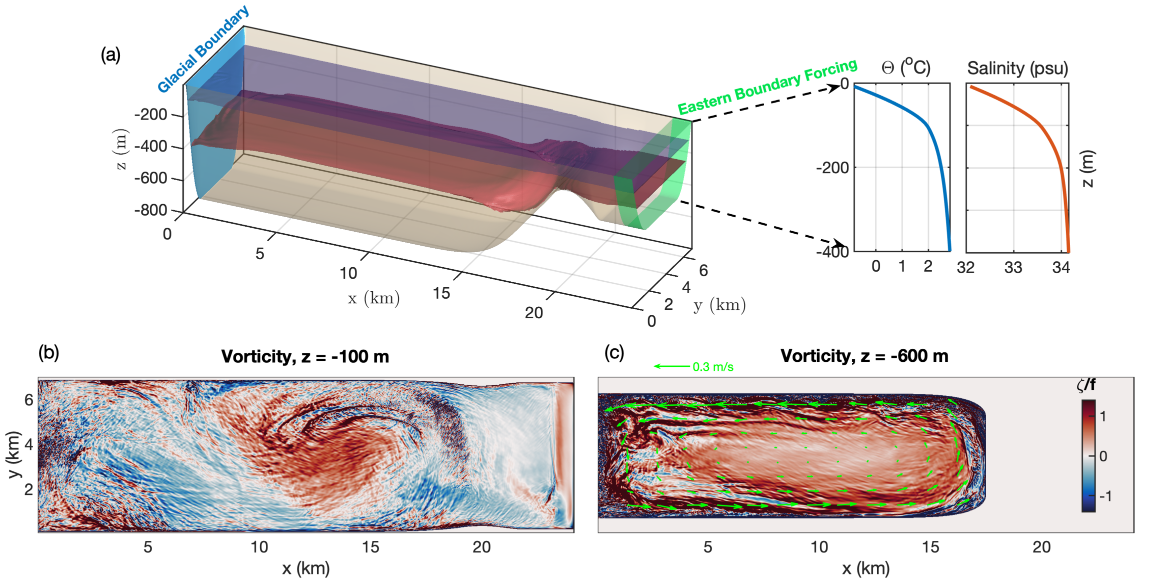

Figure 1. Reference simulation as specified in Section 2.2 showing (a) fjord geometry with two density interfaces $\sigma = 27.2$ (dark blue), 27.6 (red) kg/m^3 and the eastern boundary temperature and salinity forcing; and (b),(c) contemporaneous snapshots of normalized vorticity at $z = -100$ m and $z = -600$ m, respectively. Velocity quivers are included in panel (c).

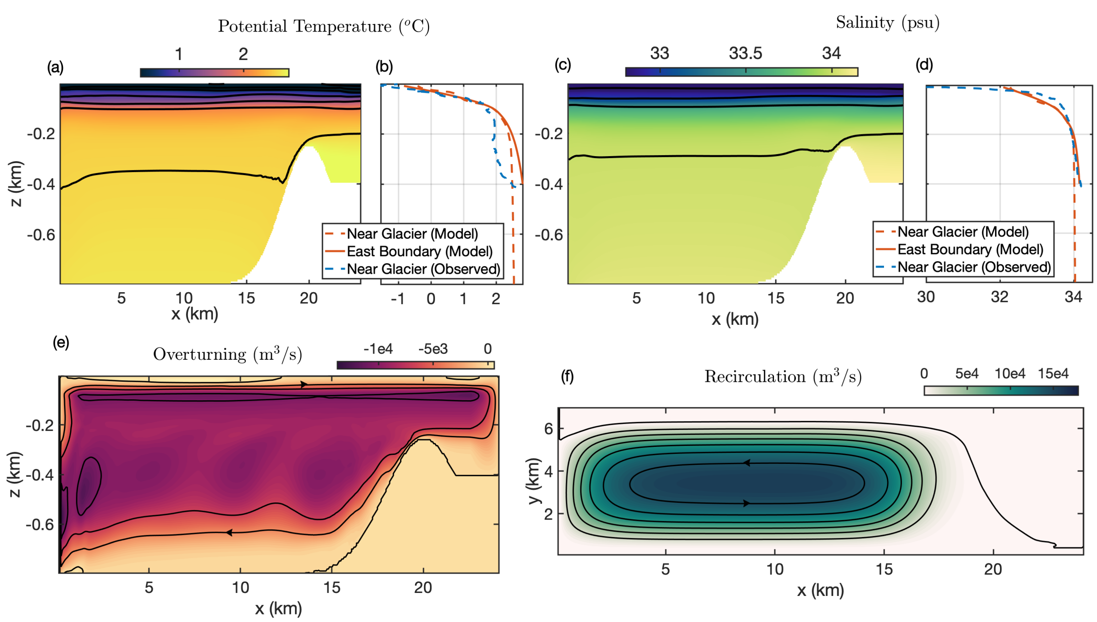

Figure 2. Time-averaged profiles of (a) meridionally-averaged temperature, (c) meridionally-averaged salinity with (b, d) model/observation comparisons using Ilulissat Icefjord data (Gladish et al., 2015; Straneo & Cenedese, 2015), and (e) meridionally-integrated overturning streamfunction, and (f) vertically-integrated recirculation strength over the bottom 600 m. The contour spacings are 0.5 °C, 0.5 psu, 3×10^3 m^3/s, and 2×10^4 m^3/s, in panels (a)-(d) respectively.

On the western boundary, the model is forced by a subglacial discharge plume parameterization at the fjord midpoint ($x = 0$, $y = W/2$) and a face-wide melt plume parameterization across the glacial face. Both plume parametrizations are based on buoyant plume theory, as described in Cowton et al. (2015). The plume parameterization solves 1D equations for mass and momentum conservation vertically along the plume, while heat and salt evolve in response to advection, entrainment of ambient waters, and the turbulent transfer to the ice face (Hellmer & Olbers, 1989). The plume is coupled to the circulation and stratification, allowing us to study feedbacks between plume dynamics and the fjord circulation. See supplemental materials S-1 for further dicussion of both plume parameterizations.

The model horizontal resolution is 38 m and the vertical resolution is 8 m. We use a Smagorinsky biharmonic horizontal viscosity and the K-Profile Parameterization (KPP) of the vertical viscosity and diffusivity (Smagorinsky, 1963; Large et al., 1994), in addition to a background vertical diffusivity of 10^{-6} m^2 s^{-1}. We use an f-plane approximation with a representative Coriolis parameter of $f = 1.31 \times 10^{-4}$ s^{-1}, corresponding to latitudes in central Greenland. The model experiments are run for 1 year because the fjord recirculation adjusts slowly and requires multiple months of spinup for some of the test cases, and all results shown (unless otherwise specified) are time-averaged over the last month.

2.2 A Reference Case

Fig. 1 illustrates the setup and circulation of our reference simulation. We impose a subglacial discharge plume of $Q_0 = 100$ m^3/s, as well as a face-wide melt plume. For reference, most subglacial discharge plumes around Greenland range from 0 to 1000 m^3/s with most fjords at the weaker end of this range (Mankoff et al., 2020). The reference case fjord dimensions are specified in Section 2.1 with a sill maximum at $z = -250$ m depth and a stratification similar to Ilulissat fjord (e.g., Gladish et al., 2015; Straneo & Cenedese, 2015) with no tidal forcing. The reference case parameters are shown in supplemental materials Table S1.

The vorticity snapshots at $z = -100$ m and $z = -600$ m in Fig. 1b, c suggest intense submesoscale variability based on the vorticity magnitude and structures generated near the sill overflow, boundary current, and plume outflow. At depth, the sill-crossing overflow (located at $x = 18.5$ km) drives energetic small-scale variability and vorticity. The overflow also feeds a cyclonic boundary current, which periodically becomes unstable and sheds eddies into the interior (see supplemental materials Fig. S1). At shallower depths, the plume outflow is the dominant source of variability and is greatest at the neutral buoyancy depth (near $z = -100$ m). The intrafjord submesoscale variability likely plays an important role in fjord stratification and mixing, circulation, and melt rates, but a more complete exploration will be deferred to a future study.

To illustrate the simulated fjord state, in Fig. 2 we plot profiles of time- and meridionally-averaged potential temperature and salinity, and compare them with observations from Illulisat Icefjord (Gladish et al., 2015; Straneo & Cenedese, 2015). The profiles of potential temperature and salinity at the ice face vs. the mouth of the fjord (panels (b) and (d)) show the effect of the water mass transformation driven by the near-glacier plumes. The modification of the inflowing water properties is more pronounced in the observations (Beaird et al., 2017) because we use a smaller discharge in our reference simulations than is observed in Illulisat Icefjord.

We quantify the fjord overturning circulation via the overturning streamfunction (Fig. 2e), which is calculated via

$$\psi(x,z) = \int_0^W \int_{z_B(x,y)}^z \overline{u} \, \mathrm{d}z' \, \mathrm{d}y' \,. \tag{1}$$

Here, $\overline{u}$ is the time-averaged velocity in the x-direction (and defined to be 0 outside the bowl-shaped domain) and $z_B(x,y)$ is the bathymetric elevation. To quantify the horizontal recirculation, we first calculate the horizontal quasi-streamfunction

$$\Psi(x,y,z) = \int_0^y \overline{u}\,\mathrm{d}y'\,, \tag{2}$$

which is an approximation to the 3D streamfunction and is further discussed in supplemental materials S-2. We quantify the strength of the horizontal recirculation via the maximum value of the horizontal quasi-streamfunction in the region between the glacier face and the sill maximum:

$$R(z) = \max_{0<x<20\,\mathrm{km}} \{\Psi(x,y,z)\}\,. \tag{3}$$

The vertically-integrated recirculation strength (over the bottom 600 m) is shown in Fig. 2f. The overturning and recirculation observed in our model results are idealized versions of the complex circulation observed in fjords with real geometries, but magnitudes are similar to those observed in nature (see Slater et al. (2018), Straneo and Cenedese (2015), and references therein).

3 Controls on Fjord Circulation and Glacial Melt

In order to understand the interaction of fjord circulation and glacial melt rate, we conduct a suite of experiments to test the effects of varying the glacial boundary layer parameterizations, discharge plume strength, geometric constraints, stratification, and tides. A complete list of the parameter ranges is shown in supplemental materials Table S1.

To understand the effect of the glacial face plumes on the fjord circulation and its feedback on melt rates, we compare four cases: the reference case and three different melt parameterizations, as listed in supplemental materials Table S1. The reference case ($\mathrm{Q_{100}M_P}$) includes a subglacial discharge plume with $Q_0 = 100$ $\mathrm{m^3/s}$ and a melt plume representing the face-wide melt (which for comparison, contributes a freshwater flux of approximately 40 $\mathrm{m^3/s}$). We additionally test three cases: (1) only the melt plume and no discharge ($\mathrm{Q_0M_P}$), (2) a boundary layer melt parameterization and no discharge ($\mathrm{Q_0M_{BL}}$, using the 3-equation thermodynamics with no melt plume, based on Hellmer and Olbers (1989)), and (3) a discharge plume only ($\mathrm{Q_{100}}$).

Fig. 3 shows how the near-glacier meridionally-integrated overturning streamfunction (using ψ from Eq. (1) and zonally-averaging over the near-glacier region, $0 < x < 5$ km), recirculation strength (R, using Eq. (2)), and meridionally-averaged melt rate (M) vary for each of these four cases. The overturning, recirculation, and melt rate are comparatively negligible for the boundary layer-only case $\mathrm{Q_0M_{BL}}$ because it does not include entrainment into the melt plume, which drives most of the overturning in the $\mathrm{Q_0M_P}$ case. The overturning circulation of the $\mathrm{Q_0M_P}$ case peaks at a depth of -500 m, while the $\mathrm{Q_{100}}$ case peaks at the discharge plume neutral buoyancy depth of -100 m. The two plumes are approximately additive, i.e., the melt plume-only and discharge plume-only experiments can be added together to approximately obtain the overturning circulation in the reference case, which utilizes both plumes.

Fig. 3 suggests that there is an approximate correlation between overturning, recirculation, and melt rate with depth, which we will discuss further in Section 4. Contrary to expectations that discharge plumes (when active) drive a majority of the melt (Straneo & Cenedese, 2015), the melt plume case shows a total melt rate that is approximately 70% of the reference case melt rate. However, the rate of undercutting (defined here as the average melt rate over the bottom 200 m) for the two cases are nearly equal because although the overturning is weaker for this case, it is located deeper in the water column, where the warmer water recirculation drives a significant percentage of the

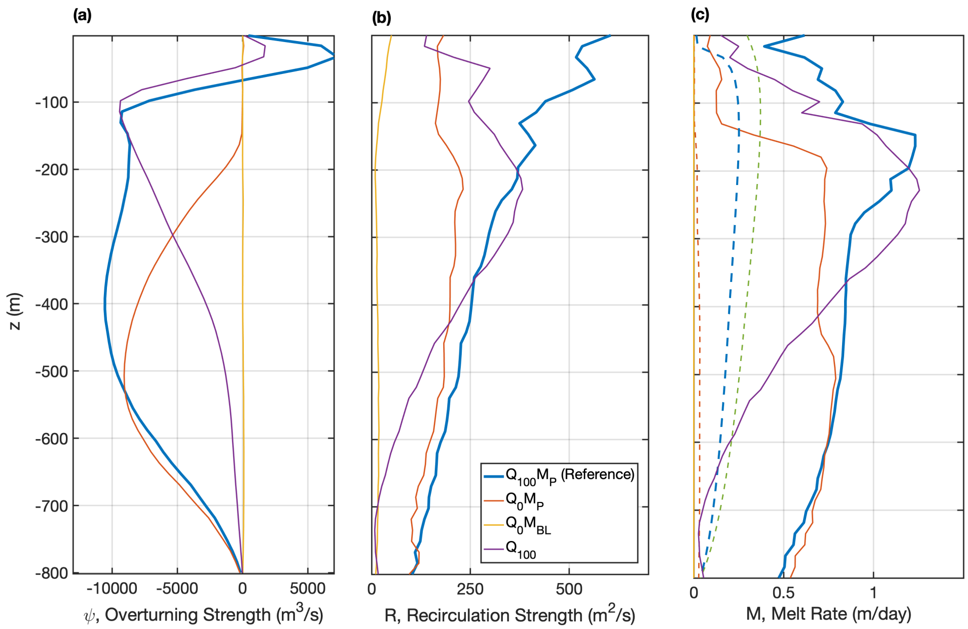

Figure 3. Profiles of (a) meridionally-integrated overturning streamfunction, (b) recirculation strength (as defined in Section 2.2), and (c) meridionally-averaged melt rate for the reference case ($Q_{100}M_P$), a melt plume only case (Q_0M_P), a boundary layer melt parameterization case (Q_0M_{BL}), and subglacial discharge only case (Q_{100}). The dotted lines in the melt rate panel show the direct contribution of the subglacial discharge plume to the meridionally-averaged melt rate.

melt rate. By comparison, the discharge plume-only case only accounts for 40% of the reference case melt rate because the overturning is located at shallower depths. Note also that most of the discharge plume-driven melt occurs over the face-wide area instead of the area where the plume is in contact with the glacial face (see Fig. 3c).

The sensitivity of the overturning, recirculation, and melt rates to discharge strength, sill height, fjord depth and width, stratification, and tides are also important and similarly show a correlation between vertical profiles of overturning, recirculation, and melt rate (see supplemental materials Figs. S2-S6 parameter sensitivity cross-section plots of temperature, salinity, overturning, recirculation, and melt rates). An important takeaway is that increasing the discharge strength leads to diminishing increases in circulation strength and melt, i.e., increasing discharge has a strong effect for weaker discharge rates, but a significantly weaker effect on melt rates beyond the discharge rate of $Q = 100$ m^3/s in the reference case. Increasing the discharge by an extreme factor of 10 (the $Q_{1000}M_P$ case) relative to the reference case increases the overturning by a factor a 2.5, but this only increases the melt rate by 30%. The reason for the diminished importance of discharge-driven melt is that increases in discharge primarily amplifies the shallow overturning and recirculation, which has a smaller impact on the overall melt rate due to the colder waters present at these depths.

4 Linking Fjord Renewal, Horizontal Circulation, and Melt

In order to understand the sensitivity of glacial melt rates to fjord parameters, we extend previous theories (Zhao et al., 2021) to relate the fjord overturning, recirculation, and melt to the parameters studied in Section 3.

4.1 Overturning Theory

Our theory for the overturning circulation uses the sum of the discharge plume entrainment and the melt plume entrainment (Morton et al., 1956; Cowton et al., 2015; Straneo & Cenedese, 2015):

$$\psi(x=0,z) \approx \beta_p B^{1/3}(z-z_B)^{5/3} + \beta_m W \left(\frac{\rho_w g_0'}{\rho_i}\right)^{1/3} M_0^{1/3}(z-z_B)^{4/3}\,. \tag{4}$$

Here, $\beta_p = (6/5)(9/5)^{1/3}\pi^{1/3}\epsilon^{4/3}$ (entrainment factor for a half-cone plume) and $\beta_m = (3/4)(4/5)^{1/3}\epsilon^{2/3}$ (entrainment factor for a sheet plume), which depend on an experimentally-derived entrainment coefficient, $\epsilon = 0.13$ (Linden, 2000). Additionally, M_0 is the melt rate (assumed to be constant with depth in the uniform density region) and ρ_w and ρ_i are the density of fresh water and ice, respectively. The discharge plume buoyancy flux $B(z) = g'Q$ varies with depth, but assuming an approximately uniform background density (ρ) below the neutral buoyancy depth yields $B \approx B_0 = g_0'Q_0$, where B_0 is the buoyancy flux at the plume source, Q_0 is the subglacial discharge rate, and the reduced gravity is $g_0' = g(\rho-\rho_w)/\overline{\rho}$. The neutral buoyancy depth of the discharge plume is primarily dependent on background stratification and weakly sensitive to the water mass transformation rates.

The melt plume buoyancy flux (last term in Eq. (4)) uses a simplified depth-constant melt rate M_0, but this can be extended to a depth-varying melt rate $M(z)$ and both the discharge plume and melt plume buoyancy flux contributions may be extended to depth-varying background density and solved numerically (see supplemental materials S-1 for further details). Our simulations suggest that the depth variation of $M(z)$ is proportional to the time-mean near-glacier along-face velocity $\overline{v}(z)$ via the relationship $M(z) \approx k_M \overline{v}(z)$ for a proportionality constant $k_M \approx 0.035$, which is further discussed in Section 4.3. This relationship suggests a potential feedback between melt, overturning, and horizontal recirculation.

4.2 Recirculation Theory

In order to understand the relationship between overturning and recirculation, we apply the scaling arguments from Zhao et al. (2021) based on the vorticity balance. This shows that below the neutral buoyancy depth (which can be predicted using plume theory; see supplemental materials S-1), vorticity generated by water mass transformation due to the glacial boundary conditions (both the melt plume and discharge plume) is primarily balanced by the curl of bottom drag (as evidenced by supplemental materials Fig. S7).

Based on an approximate balance between these two vorticity terms, we derive the following scaling relationship between the overturning streamfunction and recirculation

$$\langle\psi(x,z)\rangle_x \approx \frac{C_F C_d}{f L_r^2 H_b^2}\left(\int_{-H}^{z} R(z')\,\mathrm{d}z'\right)^2\,. \tag{5}$$

Here, $C_\mathrm{F} = 2(W + x_S)$ is the circumference of the fjord recirculation region, $C_d = 2\times 10^{-3}$ is the bottom drag coefficient, and the boundary current width L_r is empirically approximated by $L_r \sim (L_\mathrm{d} + W/2)/2$ for a deformation radius L_d. We use the zonal average of the overturning streamfunction $\langle\psi(x,z)\rangle_x$ over the near-plume region $0 < x < L_r$ as a numerical approximation to the plume-driven overturning $\psi(x=0,z)$ from Eq.

(4). The water column thickness of the recirculation region below the neutral depth is $H_b = H - |z_N|$, where z_N is the neutral depth and H is the depth of the fjord. See Zhao et al. (2021) for a more detailed discussion of this scaling theory.

4.3 Melt Rate Theory

In order to extend our predictions of recirculation to total melt rate, we apply another scaling approximation from Zhao et al. (2021) that relates the time-mean horizontal tangential velocity $\overline{v}(z)$ at the glacial face to the horizontal recirculation, expressed as $\overline{v}(z) \approx 2R(z)/(L_r H_b)$. Assuming that the melt rates are primarily driven by horizontal velocities, which is true for the majority of the glacial surface area, the 3-equation thermodynamics (using e.g., Hellmer and Olbers (1989), D. M. Holland and Jenkins (1999) and assuming ice temperatures that are close to boundary layer ocean temperatures) allows us to simplify this relationship to a linear melt rate $M(z)$ (in m/s) that is approximately proportional to $\overline{v}(z)$ (and thus, $R(z)$),

$$M(z) = \frac{c_w(T_p - T_b)}{L_i + c_i(T_b - T_i)} C_d^{1/2} \Gamma_T \sqrt{\overline{v^2} + \overline{w^2}} \approx \underbrace{\frac{c_w(T_p - T_b)}{L_i} C_d^{1/2} \Gamma_T}_{\equiv k_M} |\overline{v}| \tag{6}$$

where $L_i = 3.35 \times 10^5$ J kg^{-1} is the latent heat of fusion of ice, $c_i = 2 \times 10^3$ J kg^{-1} K^{-1} is the specific heat capacity of ice, $c_w = 3.974 \times 10^3$ J kg^{-1} K^{-1} is the specific heat capacity of water, $C_d = 2 \times 10^{-3}$ is the bottom drag coefficient, $\Gamma_T = 2.2 \times 10^{-2}$ is the thermal transfer constant, and T_b, T_p, T_i are the boundary layer, plume, and ice temperature, respectively. For further discussion on this melt rate approximation, see supplemental materials S-4.

4.4 Summary of Theories

We can rewrite the relationships in Eqs. (4)-(6) and the plume theory (in supplemental materials S-1) as a priori predictions for the bulk overturning, recirculation, and melt rate explicitly in terms of the subglacial discharge, fjord width and depth, stratification, and near-glacier horizontal velocity.

The bulk overturning strength prediction (i.e., the overturning streamfunction in Eq. (4) evaluated at the neutral buoyancy depth z_N) can be expressed as

$$\psi(z_N) \approx \beta_p (g_0' Q_0)^{1/3} (z_N - z_B)^{5/3} + \beta_m W \left(\frac{\rho_w g_0'}{\rho_i} \right)^{1/3} (k_M \langle \overline{v} \rangle_z)^{1/3} (z_N - z_B)^{4/3}\,. \tag{7}$$

Fig. 4a and 4b show the predicted vs. simulation-diagnosed values of the neutral buoyancy depth based on plume theory and the overturning strength, respectively. These two comparisons show that over the range of parameters, the neutral buoyancy depth is well-approximated by plume theory (see e.g., Turner (1979)), with a squared correlation coefficient of 0.92; similarly, overturning strength is well-approximated by Eq. (7), with a squared correlation coefficient of 0.89.

Using Eq. (5) and (7), we can express the depth-averaged recirculation below the neutral buoyancy depth in terms of the bulk overturning strength

$$\langle R \rangle_z \approx \left(\frac{\psi(z_N) f L_r^2}{C_F C_d} \right)^{1/2}, \tag{8}$$

or less accurately (as was used in the melt rate theory in Eq. (6)), the depth-averaged along-face zonal velocity

$$\langle R \rangle_z \approx L_r (H + z_N) \langle \overline{v} \rangle_z / 2\,. \tag{9}$$

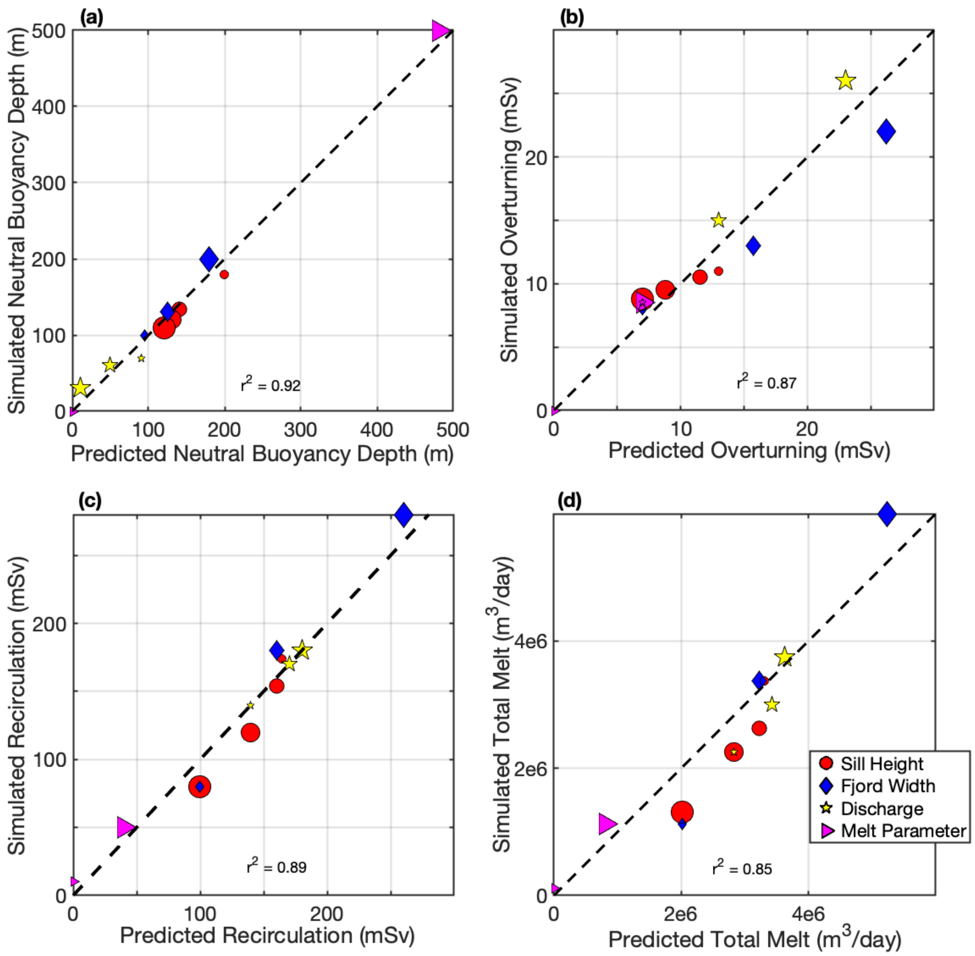

Figure 4. Simulation-diagnosed vs. theoretical predictions for (a) the neutral buoyancy depth based on plume theory, (b) the overturning circulation based on plume theory (Eq. (7)), (c) the depth-averaged recirculation based on the bulk overturning strength (Eq. (8)), and (d) the overall glacial melt rate based on the recirculation theory (Eq. (11)).

We note that equating the approximations in Eq. (8) and (9) allows us to relate the bulk overturning to the depth-averaged near-glacier along-face velocity,

$$\langle \overline{v} \rangle_z \approx \frac{2f\psi(z_N)}{C_F C_d (H + z_N)}\,, \tag{10}$$

thereby removing the dependence of these theories on $\langle \overline{v} \rangle_z$, which is an essential (albeit less accurate) step to making the melt theory fully predictive i.e., without requiring a priori knowledge of the along-glacier velocity.

Fig. 4c shows a comparison between the predicted depth-averaged recirculation below the neutral buoyancy depth using Eq. (8) and the corresponding simulation-diagnosed recirculation using Eq. (2). The recirculation above the neutral buoyancy depth is not included since vorticity advection primarily balances water mass transformation above this depth and the assumptions used for the scaling arguments used to derive Eqs. (5) and (8) no longer apply. Additionally, the melt rates in this region only account for a small percentage of the overall melt rate since the outflowing glacially-modified water masses are much colder. However, the recirculation at depths between the sill maximum and the neutral buoyancy depth are taken into account in Eqs. (5) and (8). Fig. 4c shows that over the range of parameters, recirculation varies over a large range, but is well-approximated by this simple scaling argument, with a squared correlation coefficient of 0.89.

Finally, the depth-averaged melt rate can be expressed as

$$\langle M \rangle_z \approx k_M \langle \overline{v} \rangle_z\,. \tag{11}$$

Fig. 4d shows a comparison between the predicted depth-averaged melt rate calculated from Eq. (11) multiplied by the glacial surface area and the corresponding value diagnosed from the simulation by integrating the melt rate over the entire glacial face. This shows that over the range of parameters, melt rate varies significantly, but is relatively well-approximately by this simple scaling argument. Although the prediction of total melt rate is less accurate (with a squared correlation coefficient of 0.85) than the predicted recirculation, this is likely because the melt rate theory requires additional approximations and assumptions. The melt rate can also be (less accurately) related to the bulk overturning strength or depth-averaged recirculation using Eqs. (10) and (9), respectively, to remove the dependence on the the near-glacier along-face velocity. The fully predictive theory for the total melt rate in terms of the overturning streamfunction by substituting Eq. (10) in Eq. (11) is compared with the simulation diagnosed melt rate in Fig. S8 (which has a squared correlation coefficient of 0.72).

5 Discussion and Conclusion

In this study, we use a high-resolution idealized model (see Section 2) to analyze the sensitivity of glacial melt to fjord circulation (in Section 3) and address an important gap in scientific understanding: how fjord circulation and glacial melt co-influence each other and how to predict their bulk values as a function of fjord parameters. To achieve this, we extended previous theories (in Section 4) to predict the overturning, recirculation, and melt rates as functions of the model fjord parameters. These relationships are summarized in Eqs. (7)-(11), which explicitly express the sensitivity of the circulation and melt to each of the fjord parameters and illustrate the melt-circulation feedback, using the near-glacier velocity as a common link.

We found that a majority of the glacial melt occurs over the entire glacial front, instead of being localized to the discharge plume. For the highest discharge case ($\mathrm{Q}_{1000}\mathrm{M}_{\mathrm{P}}$), the discharge plume region accounts for only 26% of the overall melt (and only 18% for the reference case) even though it increases the peak overturning strength by a factor of 2.5, because it confines this overturning to a narrow depth range near the neutral buoyancy depth. Most of the parameter variations we studied had a significant impact on the overall melt rate (see supplemental materials Fig. S6 for a figure showing the sensitivity of glacial melt distributions to fjord properties). These variations in melt can be theoretically related to the recirculation and overturning circulation, which in turn have two drivers: a face-wide melt plume and a discharge plume.

The discharge plume drives a shallower overturning than the face-wide melt plume and, therefore, the face-wide melt plays a significantly larger role in glacial melt because it provides a greater proportion of the deep overturning. In this deep overturning circulation, warm water masses flow toward the glacial face at a range of depths primarily in the deeper half of the fjord, and flows away in the upper half (see the $\mathrm{Q_0M_P}$ case in Fig. 2a). Our results show that over most of the fjord parameter range studied, the deep overturning within fjords is primarily driven by melt, and the overall melt is primarily driven by recirculation at depth, which is correlated with the deep overturning circulation. This glacial melt seems to be concentrated at depth due to the warm water available at these depths, where the stratification is weaker. Additionally, the warm-water renewal in the deeper waters of the fjord is more strongly controlled by face-wide melt compared to the subglacial discharge plume. This potentially has implications that fjords with weak subglacial discharge year-round or in wintertime conditions can still have substantial melt rates as long as warm water is present within the fjord. There is observational evidence that suggests this may occur in some fjords (Wood et al., 2018), but more wintertime glacial melt rate observations are needed to confirm this phenomenon.

There are numerous caveats in this study due to the limitations of our simple model configuration. These include the simplicity of fjord geometry, atmospheric forcing, vertical mixing representation, the lack of sea ice, mélange, and icebergs, which can supply substantial buoyancy input (Beaird et al., 2017). As a result of the high-resolution fjord-only domain, a caveat is the prescription of the eastern open-ocean boundary. The eastern boundary in our model is nudged to the open-ocean stratification, which is fixed for our simulation, so the boundary likely does not capture all of the variability that a fjord-shelf system would be able to include; there can be a shelf current-induced increase/decrease in the exchange between the fjord and shelf (Zhao et al., 2021). We also do not consider the effect of winds, which likely exhibits a larger effect on the shelf region via fjord overturning driven by coastal upwelling (not included in our domain), but may also directly drive fjord circulation/renewal for strong enough katabatic wind events (Zhao et al., 2021; Spall et al., 2017). Although this choice is an imperfect one, the eastern boundary is nudged to fjord mouth observations (from Gladish et al. (2015)); in reality, a domain that includes the shelf would likely establish a balance between the shelf stratification and near-glacial stratification to set the stratification at the fjord mouth (e.g., Zhao et al. (2021)). Also, in our glacial boundary parameterization, the melt rates are calculated using the closest grid point of horizontal and vertical fjord velocities, which is an imperfect representation; in general, a better understanding and representation of the ice-ocean boundary layer needed to improve glacial melt rate estimates.

Following this study, there are a number of open questions that require further attention. Additional work is needed to investigate the submesoscale phenomenology and the distribution of mixing within the fjord. Another future avenue is to investigate boundary layer parameterizations at the glacial face and the interaction of submesoscale-microscale dynamics. A final avenue is to investigate the interaction between circulation and melt in more realistic regional models and the co-interaction of multiple neighboring fjords.

Acknowledgments

This material is based in part upon work supported by the NASA FINESST Fellowship under Grant 80NSSC20K1636 and the National Science Foundation under Grant

OCE-1751386. This work used the Extreme Science and Engineering Discovery Environment (XSEDE, Towns et al. (2014)), which is supported by National Science Foundation grant number ACI-1548562. The MITgcm model configuration, test case, and modified plume parameterization (a slightly modified version of Cowton et al. (2015)) is available at: *https://doi.org/10.5281/zenodo.5214142*.

References

Bartholomaus, T. C., Larsen, C. F., & O'Neel, S. (2013). Does calving matter? Evidence for signicant submarine melt. *Earth Planet. Sci. Lett.*, *380*, 21–30. doi: 10.1016/j.epsl.2013.08.014

Beaird, N., Straneo, F., & Jenkins, W. (2017). Characteristics of Meltwater Export from Jakobshavn Isbrae and Ilulissat Icefjord. *Ann. Glaciol.*, *58*(74), 107–117. doi: 10.1017/aog.2017.19

Carroll, D., Sutherland, D. A., Shroyer, E., Nash, J. D., Catania, G., & Stearns, L. A. (2017). Subglacial discharge-driven renewal of tidewater glacier fjords. *J. Geophys. Res. Oceans*, *122*, 6611–6629.

Chauché, N., Hubbard, A., Gascard, J. C., Box, J. E., Bates, R., & Koppes, e. a., M. (2014). Ice-ocean interaction and calving front morphology at two west greenland tidewater outlet glaciers. *Cyrosphere*, *8*, 1457–1468. doi: doi.org/10.5194/tc-8-1457-2014

Cottier, F., Nilsen, F., Skogseth, R., Tverberg, V., Skardhamar, J., & Svendsen, H. (2010, 11). Arctic fjords: A review of the oceanographic environment and dominant physical processes. *Geological Society of London Special Publications*, *344*, 35–50. doi: 10.1144/SP344.4

Cowton, T., Slater, D., Sole, A., Goldberg, D., & Nienow, P. (2015). Modeling the impact of glacial runoff on fjord circulation and submarine melt rate using a new subgrid-scale parameterization for glacial plumes. *J. Geophys. Res. Oceans*, *120*, 796–812.

Cowton, T., Sole, A. J., Nienow, P. W., Slater, D. A., & Christoffersen, P. (2018). Linear response of east greenland's tidewater glaciers to ocean/atmosphere warming. *Proc. Natl. Acad. Sci. (USA)*, *115*(31), 7907–7912. doi: 10.1073/pnas.1801769115

Farmer, D., & Freeland, H. (2021). The physical oceanography of fjords. *Prog. Oceanogr.*, *12*, 147–220.

Fried, M. J., Catania, G. A., Stearns, L. A., Sutherland, D. A., Bartholomaus, T. C., Shroyer, E., & Nash, J. (2018). Reconciling drivers of seasonal terminus advance and retreat at 13 central west greenland tidewater glaciers. *J. Geophys. Res. Earth Surface*, *123*(7), 1590–1607. doi: doi.org/10.1029/2018JF004628

Geyer, W. R., & MacCready, P. (2014). The Estuarine Circulation. *Annu. Rev. Fluid Mech*, *46*(1), 175-197. doi: 10.1146/annurev-fluid-010313-141302

Gladish, C. V., Holland, D. M., Rosing-Asvid, A., Behrens, J. W., & Boje, J. (2015). Oceanic Boundary Conditions for Jakobshavn Glacier. Part I: Variability and Renewal of Ilulissat Icefjord Waters, 200114. *J. Phys. Oceanogr.*, *45*(1), 3-32. doi: 10.1175/JPO-D-14-0044.1

Hellmer, H. H., & Olbers, D. J. (1989). A two-dimensional model for the thermohaline circulation under an ice shelf. *Antarctic Science*, *1*(4), 325–336. doi: 10.1017/S0954102089000490

Holland, D. M., & Jenkins, A. (1999). Modeling Thermodynamic Ice-Ocean Interactions at the Base of an Ice Shelf. *J. Phys. Oceanogr.*, *29*(8), 1787–1800. doi: 10.1175/1520-0485(1999)029⟨1787:MTIOIA⟩2.0.CO;2

Holland, P. R., Jenkins, A., & Holland, D. M. (2008). The response of ice shelf basal melting to variations in ocean temperature. *J. Climate*, *21*, 2258–2272. doi: 10.1175/2007JCLI1909.1

Inall, M. E., & Gillibrand, A., P. (2010). The physics of mid-latitude fjords: a review. *Geological Society of London Special Publications*, *344*, 17–33.

Jackson, R. H., Lentz, S. J., & Straneo, F. (2018). The Dynamics of Shelf Forcing in Greenlandic Fjords. *J. Phys. Oceanogr.*, *48*(11), 2799-2827. doi: 10.1175/JPO-D-18-0057.1

Jackson, R. H., Nash, J. D., Kienholz, C., Sutherland, D. A., Amundson, J. M., Motyka, R. J., ... Pettit, E. (2019). Meltwater intrusions reveal mechanisms for rapid submarine melt at a tidewater glacier. *Geophys. Res. Lett.*. doi: 10.1029/2019GL085335

Linden, P. F. (2000). *Convection in the environment. In Perspectives in Fluid Dynamics, ed. GK Batchelor, HK Moffat, MG Worster.* Cambridge, U.K.: Cambridge University Press.

Magorrian, S. J., & Wells, A. J. (2016). Turbulent plumes from a glacier terminus melting in a stratified ocean. *J. Geophys. Res. Oceans*, *121*(7), 4670–4696. doi: 10.1002/2015JC011160

Mankoff, K. D., Noël, B., Fettweis, X., Ahlstrm, A. P., Colgan, W., Kondo, K., ... Fausto, R. S. (2020). Greenland liquid water discharge from 1958 through 2019. *Earth Syst. Sci. Data*, *12*, 2811–2841. doi: doi.org/10.5194/essd-12-2811-2020

Marshall, J. A., Hill, C., Perelman, L., & Heisey, C. (1997). A finite-volume, incompressible navier stokes model for studies of the ocean on parallel computers. *J. Geophys. Res.*, *102 (C3)*, 5753–5766.

Morlighem, M., Bondzio, J., Seroussi, H., Rignot, E., Larour, E., Humbert, A., & Rebuffi, S. (2016). Modeling of store gletschers calving dynamics, west greenland, in response to ocean thermal forcing. *Geophys. Res. Lett.*, *43*, 2659–2666. doi: doi.org/10.1002/2016GL067695

Morton, B. R., Taylor, G. I., & Turner, J. S. (1956). Turbulent gravitational convection from maintained and instantaneous sources. *Proceedings of the Royal Society of London. Series A. Mathematical and Physical Sciences*, *234*(1196), 1-23. doi: 10.1098/rspa.1956.0011

Rignot, E., Fenty, I., Xu, Y., Cai, C., & Kemp, C. (2015). Undercutting of marine-terminating glaciers in west greenland. *Geophys. Res. Lett.*, *42*(14), 5909–5917. doi: doi.org/10.1002/2015GL064236

Sciascia, R., Straneo, F., Cenedese, C., & Heimbach, P. (2013). Seasonal variability of submarine melt rate and circulation in an East Greenland fjord. *J. Geophys. Res. Oceans*, *118*, 2492–2506.

Slater, D. A., Benn, D. I., Cowton, T. R., Bassis, J. N., & Todd, J. A. (2021). Calving multiplier effect controlled by melt undercut geometry. *J. Geophys. Res. Earth Surf.*, *n/a*(n/a), e2021JF006191. doi: https://doi.org/10.1029/2021JF006191

Slater, D. A., Straneo, F., Das, S. B., Richards, C. G., Wagner, T. J. W., & Nienow, P. W. (2018). Localized Plumes Drive Front-Wide Ocean Melting of A Greenlandic Tidewater Glacier. *Geophys. Res. Lett.*, *45*(22), 12,350 – 12,358. doi: 10.1029/2018GL080763

Spall, M. A., Jackson, R. H., & Straneo, F. (2017). Katabatic Wind-Driven Exchange in Fjords. *J. Geophys. Res. Oceans*, *122*(10), 8246-8262. doi: 10.1002/2017JC013026

Stigebrandt, A. (1981). A mechanism governing the estuarine circulation in deep, strongly stratified fjords. *Estuar. Coast. Mar. Sci.*, *13*, 197–211.

Straneo, F., & Cenedese, C. (2015). The Dynamics of Greenland's Glacial Fjords and Their Role in Climate. *Annu. Rev. Mar. Sci.*, *7*(1), 89-112. doi: 10.1146/annurev-marine-010213-135133

Straneo, F., & Heimbach, P. (2013). North Atlantic Warming and the Retreat of Greenland's Outlet Glaciers. *Nature*, *504*(7478), 36–43. doi: https://doi.org/10.1038/nature12854

Towns, J., Cockerill, T., Dahan, M., Foster, I., Gaither, K., Grimshaw, A., … Wilkins-Diehr, N. (2014, Sept). XSEDE: Accelerating scientific discovery. *Computing in Science & Engineering*, *16*(5), 62-74. doi: 10.1109/MCSE.2014.80

Turner, J. S. (1979). *Buoyancy effects in fluids. Cambridge University Press Paperback.*

van den Broeke, M. R., Enderlin, E. M., Howat, I. M., Munneke, P. K., Noël, B. P. Y., van de Berg, W. J., … Wouters, B. (2016). On the recent contribution of the Greenland ice sheet to sea level change. *The Cryosphere*, *10*, 1933–1946. doi: 10.5194/tc-10-1933-2016

Wagner, T. J. W., James, T. D., Murray, T., & Vella, D. (2016). On the role of buoyant flexure in glacier calving. *Geophys. Res. Lett.*, *43*(1), 232–240A. doi: doi.org/10.1002/2015GL067247

Wood, M., Rignot, E., Fenty, I., An, L., Bjørk, A., van den Broeke, M., … Zhang, H. (2021). Ocean forcing drives glacier retreat in Greenland. *Science Advances*, *7*(1). doi: 10.1126/sciadv.aba7282

Wood, M., Rignot, E., Fenty, I., Menemenlis, D., Millan, R., Morlighem, M., … Seroussi, H. (2018). Ocean-Induced Melt Triggers Glacier Retreat in Northwest Greenland. *Geophys. Res. Lett.*, *45*(16), 8334–8342. doi: 10.1029/2018GL078024

Xu, Y., Rignot, E., Menemenlis, D., & Koppes, M. (2012). Numerical experiments on subaqueous melting of Greenland tidewater glaciers in response to ocean warming and enhanced subglacial discharge. *Ann. Glaciol.*, *53 (60)*, 229–234.

Zhao, K. X., Stewart, A. L., & McWilliams, J. C. (2019). Sill-Influenced Exchange Flows in Ice Shelf Cavities. *J. Phys. Oceanogr.*, *49 (1)*, 163–191. doi: 10.1175/JPO-D-18-0076.1

Zhao, K. X., Stewart, A. L., & McWilliams, J. C. (2021). Geometric Constraints on Glacial FjordShelf Exchange. *J. Phys. Oceanogr.*, *51 (4)*, 1223–1246. doi: 10.1175/JPO-D-20-0091.1

Figure 1.

(a)
Glacial Boundary
Eastern Boundary Forcing
z (m)
-200
-400
-600
-800
0
5
10
15
20
x (km)
0
2
4
6
y (km)
Θ (°C)
Salinity (psu)
0
-200
-400
0
1
2
32
33
34
z (m)
(b)
Vorticity, z = -100 m
y (km)
6
4
2
5
10
15
20
x (km)
(c)
0.3 m/s
Vorticity, z = -600 m
ζ/f
1
0
-1
5
10
15
20
x (km)

Figure 2.

Potential Temperature (^{o}C)
1
2
(a)
(b)
-0.2
-0.4
-0.6
z (km)
5
10
15
20
x (km)
-1
0
1
2
Near Glacier (Model)
East Boundary (Model)
Near Glacier (Observed)
Salinity (psu)
33
33.5
34
(c)
(d)
30
32
34
(e)
Overturning (m^3/s)
-1e4
-5e3
0
(f)
Recirculation (m^3/s)
0
5e4
10e4
15e4
y (km)
6
4
2

Figure 3.

(a)
(b)
(c)
z (m)
-100
-200
-300
-400
-500
-600
-700
-800
-10000
-5000
0
5000
ψ, Overturning Strength (m^3/s)
0
250
500
R, Recirculation Strength (m^2/s)
0
0.5
1
M, Melt Rate (m/day)
$Q_{100}M_P$ (Reference)
Q_0M_P
Q_0M_{BL}
Q_{100}

Figure 4.

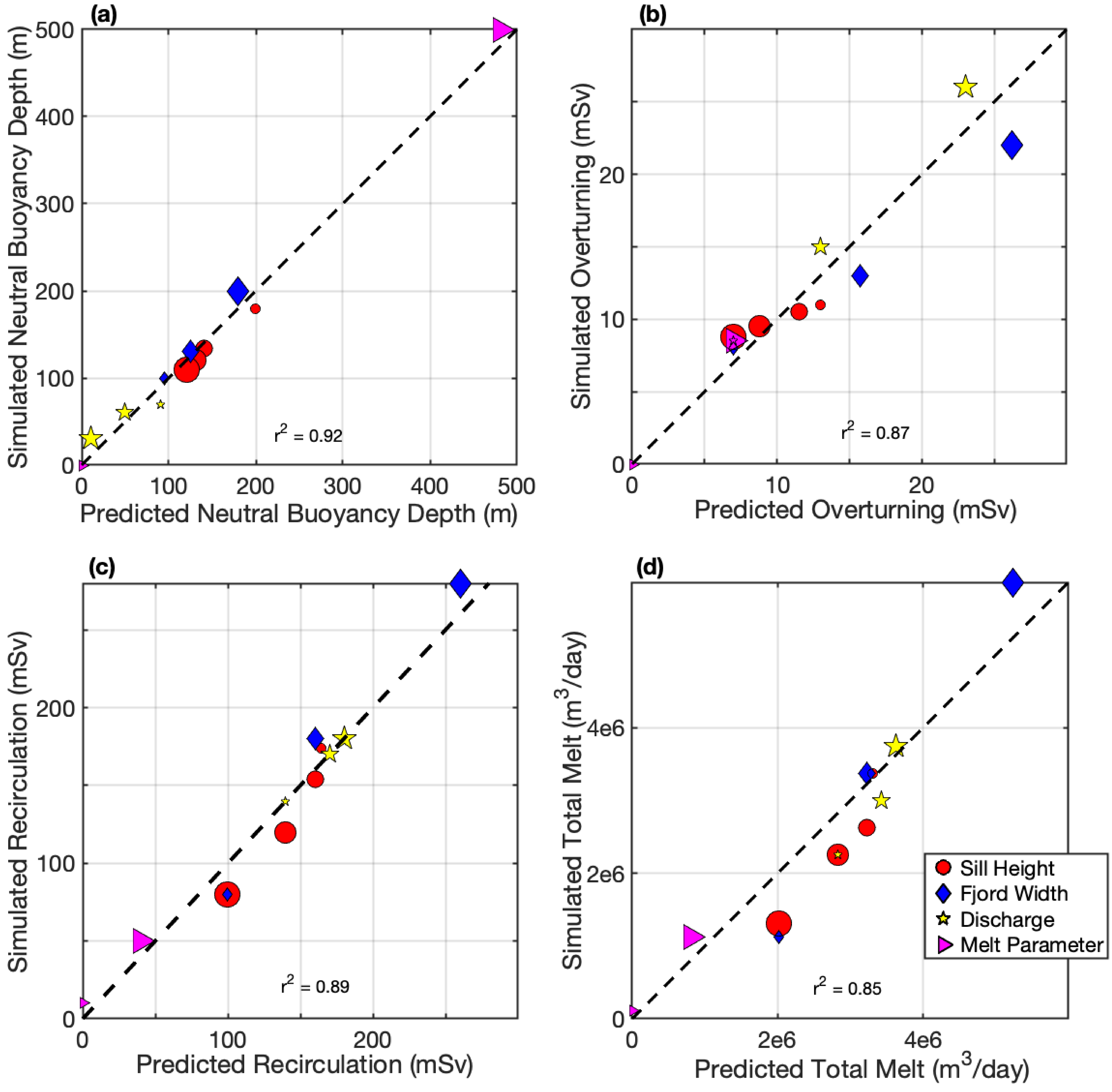

(a)
Simulated Neutral Buoyancy Depth (m)
Predicted Neutral Buoyancy Depth (m)
r^2 = 0.92
(b)
Simulated Overturning (mSv)
Predicted Overturning (mSv)
r^2 = 0.87
(c)
Simulated Recirculation (mSv)
Predicted Recirculation (mSv)
r^2 = 0.89
(d)
Simulated Total Melt (m^3/day)
Predicted Total Melt (m^3/day)
r^2 = 0.85
Sill Height
Fjord Width
Discharge
Melt Parameter

Supporting Information for "Linking Overturning, Recirculation, and Melt in Glacial Fjords"

Ken X. Zhao[1], Andrew L. Stewart[1], and James C. McWilliams[1]

[1]Department of Atmospheric and Oceanic Sciences, University of California, Los Angeles

Contents of this file

S-1. Model Setup and Plume Parameterizations

The model used in the study is the Massachusetts Institute of Technology General Circulation Model (MITgcm), which is available at *mitgcm.org*. Using this model, we solve the hydrostatic, Boussinesq primitive equations with a nonlinear equation of state based on Jackett and McDougall (1995). For the cases with tides (see Table S1), we use a barotropic tidal velocity (with magnitudes of 0 to 0.1 m/s) with a semi-diurnal frequency.

The plume parameterizations that we implement in the MITgcm model configuration is a slightly modified version of that proposed by Cowton, Slater, Sole, Goldberg, and Nienow (2015), optimized to work efficiently in high resolution simulations, and is available at: *https://doi.org/10.5281/zenodo.5214142*. This is identical to the parameterization package detailed in Cowton et al. (2015), except that we redistribute the buoyancy anomalies from the solutions to the discharge plume equations over a 10-gridpoint radius semi-circle in the horizontal and apply a 3-gridpoint smoothing in the vertical while conserving the overall buoyancy anomaly and entrainment. This prevents prohibitive restrictions set by the Courant-Friedrichs-Lewy (CFL) condition on the model timestep in our high resolution simulations as well as spurious mixing caused by sharp gradients in the forcing at the gridscale.

The basic formulas for the vertical volume flux via entrainment for a point source plume (representing the discharge plume) and a sheet plume (representing the distributed melt plume) that are used in these plume parameterizations (as well as the theory in Section 4) can be derived from classic self-similarity and entrainment assumptions (see e.g., Morton, Taylor, and Turner (1956)). To provide context for our theory, the following is a brief overview of the fundamental aspects of plume theory.

An idealized axisymmetric turbulent plume can be defined in terms of parameters B (buoyancy flux) and r (radial length scale), which are functions of z (height above the source). For a constant background density, it is often assumed that plume profiles are self-similar and dimensional analysis can be used to find the vertical velocity w, reduced gravity g', and r as a function of z. Alternatively, for background density profiles that vary with height, and the plume parameterization used in our model configuration, the vertical properties of the plume are found numerically by solving a set of differential equations, i.e., the conservation of mass, momentum, and buoyancy flux (based on Turner (1979)):

$$\frac{\partial m}{\partial z} = 2\alpha m/r\,, \tag{1a}$$

$$\frac{\partial mw}{\partial z} = mg'/w\,, \tag{1b}$$

$$\frac{\partial mg'}{\partial z} = -mN^2(z)\,, \tag{1c}$$

for a plume entrainment mass flux $m = r^2 w$. A similar set of equations can also be derived for the front-wide melt plume by imposing a distributed buoyancy flux and can also be solved numerically (see Turner (1979)). For a more complete plume formulation which includes temperature, salinity, and density profiles that vary with depth (such as the one implemented in our model), see Cowton et al. (2015).

In order to arrive at the simplifications to the overturning theory discussed in Section 4 (which are discharge- and melt plume-driven), we can approximate the solution to Eqs. (1a)-(1c) by assuming an approximately uniform density below the depth of neutral buoyancy (which is a fairly accurate approximation given the weak stratification below the neutral buoyancy depth in many of Greenland's fjords; see e.g., Straneo and Cenedese (2015)). This approximation allows the buoyancy flux equation (Eq. (1c)) to be simplified to

$$B = mg'\,, \tag{2}$$

which results in the self-similar discharge plume solutions used in Section 4.1 (see Straneo and Cenedese (2015) for a discussion). The melt rate that is used for the buoyancy flux of the melt-driven plume can be approximated to be uniform with depth for simplicity (approximately a vertical mean) for the simplified overturning circulation approximation theory in Section 4.1, which allows for a similarity solution for the melt plume component used in Eq. (4) (in the main text).

S-2. Quasi-Streamfunction Discussion

We note that the quasi-streamfunction defined in Eq. (3) (in the main text) is only approximately equal to the 3D streamfunction, which can be defined via the relationship $(u, v, w) = \nabla \times \Psi_3$. The horizontal velocity field (u, v) is unlikely to be exactly nondivergent anywhere, but over most of the fjord, the horizontal velocity field is approximately nondivergent, i.e., the x- and y-components of the streamfunction vector are approximately zero and the flow is approximately described by the z-component of the streamfunction. The lack of boundary-incident streamlines in Fig. 2e in the main text and Fig. S4 suggests that the horizontal velocity field is indeed approximately nondivergent. Since the calculation of this quasi-streamfunction is calculated by taking the integral in the across-fjord direction, the interior quasi-streamfunction is largely unaffected by the eastern and western boundary nudged regions.

S-3. Fjord Circulation and Melt Sensitivity to Discharge Plume Strength, Geometry, Stratification, and Tides

This section provides additional exposition of the dependence of the fjord circulation and melt on the various model control parameters discussed in Section 3 of the main text. Figs. S2-S6 shows the time-averaged meridionally-averaged temperature and salinity, overturning circulation, and vertically-integrated horizontal recirculation, and glacial melt rates for 9 endmember cases. All of the parameter variations seen here substantially influence the circulation and/or melt rate and suggest that these properties are all likely to be important when considering overturning, recirculation, and melt rates in real fjord systems.

The overturning circulation in the greatest discharge strength case $Q_0 = 1000$ m^3/s (Fig. S4d) increases by a factor of 2.5 compared to the $Q_0 = 100$ m^3/s case (Fig. S4c), but the overall melt rate only increases by 30% (Fig. S6c, d). Similarly to the reference case, the discharge plume and melt plume with a high discharge ($Q_0 = 1000$ m^3/s) is also additive, but the discharge-driven shallow overturning cell dominates the peak overturning strength (Fig. S4d). The increase in discharge primarily increases the magnitude of the shallow overturning circulation, which increases the shallow recirculation. An important takeaway is that at these depths, the recirculation (in Fig. S5d) has a much smaller impact on the overall melt rate.

Decreasing the sill height removes barriers of warm water access to the fjord (Fig. S2e) and increases melt rates by 20% for the case with no sill relative to the reference case (Fig. S6e). Increasing the fjord width from 6 km to 15 km approximately doubles the recirculation (Fig. S5f) and also doubles the melt rates (Fig. S6f) for the $W = 25$ km case. Decreasing the fjord depth weakens the overturning circulation (Fig. S4g) and melts a smaller cross-sectional glacial surface area, which results in a 25% decrease in melt rate for the shallow depth case ($H_{\mathrm{fj}} = 600$ m) compared to the reference case (Fig. S5g).

Increasing the surface stratification slightly strengthens the deep overturning (Fig. S4h), recirculation (Fig. S5h), and therefore, melt rate (Fig. S6h). The strength of the tides can also amplify the overturning circulation at the glacial face at depths near the sill maximum depth and can lead to a 30% increase in overall melt rates (Fig. S6i) for a barotropic tidal amplitude of 0.1 m/s.

S-4. Melt Rate Theory Approximations

The expressions and approximations used in Section 4.3 on the melt rate theory are a variation of the three-equation system of equations (Hellmer & Olbers, 1989; Holland & Jenkins, 1999) which describes the thermodynamical equilibrium at the ice-ocean interface. This equilibrium can be expressed using approximate heat and salt conservation and the linearized freezing temperature of seawater,

$$M(L_i + c_i(T_b - T_i)) = \gamma_T c_w (T_p - T_b) \tag{3a}$$

$$M S_b = \gamma_S (S_p - S_b)\,, \tag{3b}$$

$$T_b = \lambda_1 S_b + \lambda_2 + \lambda_3 z\,, \tag{3c}$$

where $M, L_i, c_w, c_i, C_d, T_b, T_i, T_p$ are defined in Section 4.3, S_p is the plume salinity, S_b is the boundary layer salinity, γ_S is the turbulent salt transfer coefficient, and $\lambda_1 = -5.73 \times 10^{-2}$ °C psu^{-1}, $\lambda_2 = 8.32 \times 10^{-2}$ °C, and $\lambda_3 = 7.61 \times 10^{-4}$ °C m^{-1} are the freezing point slope, offset, and depth. These empirical values are consistent with those used in previous studies (Sciascia et al., 2013; Cowton et al., 2015). Recent parameterizations of the turbulent transfer coefficients (Jenkins et al., 2010) express the turbulent transfer coefficients in terms of near-glacial ocean velocities as

$$\gamma_T = C_d^{1/2} \Gamma_T \sqrt{v^2 + w^2}\,, \tag{4a}$$

$$\gamma_S = C_d^{1/2} \Gamma_S \sqrt{v^2 + w^2}\,, \tag{4b}$$

with C_d, Γ_T, v, w as defined in Section 4.3, and $\Gamma_S = 6.2 \times 10^{-4}$ is the salt transfer constant.

For simplicity, our theory in Section 4.3 for the melt rate M only uses Eqs. (3a) and (4a), since the plume and boundary layer temperature can be evaluated in our model directly (and does not vary significantly over the cases tested). We can then integrate the melt rate outside the discharge plume regions (which allows us to simplify $\sqrt{v^2 + w^2}$ to v) since this is where the majority of the melt occurs.

References

Cowton, T., Slater, D., Sole, A., Goldberg, D., & Nienow, P. (2015). Modeling the impact of glacial runoff on fjord circulation and submarine melt rate using a new subgrid-scale parameterization for glacial plumes. *J. Geophys. Res. Oceans*, *120*, 796–812.

Hellmer, H. H., & Olbers, D. J. (1989). A two-dimensional model for the thermohaline circulation under an ice shelf. *Antarctic Science*, *1*(4), 325–336. doi: 10.1017/S0954102089000490

Holland, D. M., & Jenkins, A. (1999). Modeling Thermodynamic Ice-Ocean Interactions at the Base of an Ice Shelf. *J. Phys. Oceanogr.*, *29*(8), 1787–1800. doi: 10.1175/1520-0485(1999)029⟨1787:MTIOIA⟩2.0.CO;2

Jackett, D. R., & McDougall, T. (1995). Minimal adjustment of hydrographic profiles to achieve static stability. *J. Atmos. Ocean. Technol.*, *14*(4), 381–389.

Jenkins, A., Dutrieux, P., Jacobs, S., McPhail, S., Perrett, J., Webb, A., & White, D. (2010). Observations beneath Pine Island Glacier in West Antarctica and implications for its retreat. *Nat. Geosci.*, *3*, 468–472.

Morton, B. R., Taylor, G. I., & Turner, J. S. (1956). Turbulent gravitational convection from maintained and instantaneous sources. *Proceedings of the Royal Society of London. Series A. Mathematical and Physical Sciences*, *234*(1196), 1-23. doi: 10.1098/rspa.1956.0011

Sciascia, R., Straneo, F., Cenedese, C., & Heimbach, P. (2013). Seasonal variability of submarine melt rate and circulation in an East Greenland fjord. *J. Geophys. Res. Oceans*, *118*, 2492–2506.

Straneo, F., & Cenedese, C. (2015). The Dynamics of Greenland's Glacial Fjords and Their Role in Climate. *Annu. Rev. Mar. Sci.*, *7*(1), 89-112. doi: 10.1146/annurev-marine-010213-135133

Turner, J. S. (1979). *Buoyancy effects in fluids. Cambridge University Press Paperback.*

Zhao, K. X., Stewart, A. L., & McWilliams, J. C. (2021). Geometric Constraints on Glacial Fjord–Shelf Exchange. *J. Phys. Oceanogr.*, *51 (4)*, 1223–1246. doi: 10.1175/JPO-D-20-0091.1

Name	*Parameter*	*Test Cases*	*Test Name*	*Units*
Sill Height	H_S	[0, **150**, 200, 250]	[S_0, - , S_{150}, S_{200}, S_{250}]	m
Fjord Width	W_{fj}	[4,**6**,9,15]	[W_4, - , W_9, W_{15}]	km
Fjord Depth	H_{fj}	[600,**800**,1000]	[D_{600}, - , D_{1000}]	m
Fjord Length (constant)	L_{fj}	25		km
Subglacial Discharge	Q_0	[0, **100**, 300, 1000]	[$Q_0, Q_{100}, Q_{300}, Q_{1000}$]	m^3/s
Melt Parameterization		[No melt, Boundary Layer Melt, **Melt Plume**]	[- , M_{BL}, M_P]	
Stratification	$\rho_3 - \rho_2$	[0.25, **0.45**, 0.65]	[$\Delta\rho_{0.25}$, - , $\Delta\rho_{0.65}$]	kg/m^3
Tidal Amplitude	u_{tide}	[**0**, 0.05, 0.1]	[- , $T_{0.05}$, $T_{0.1}$]	m/s

TABLE 1. Summary of key fjord parameters and test cases for the numerical simulations. All variables are independently varied relative to the reference case (in bold text).

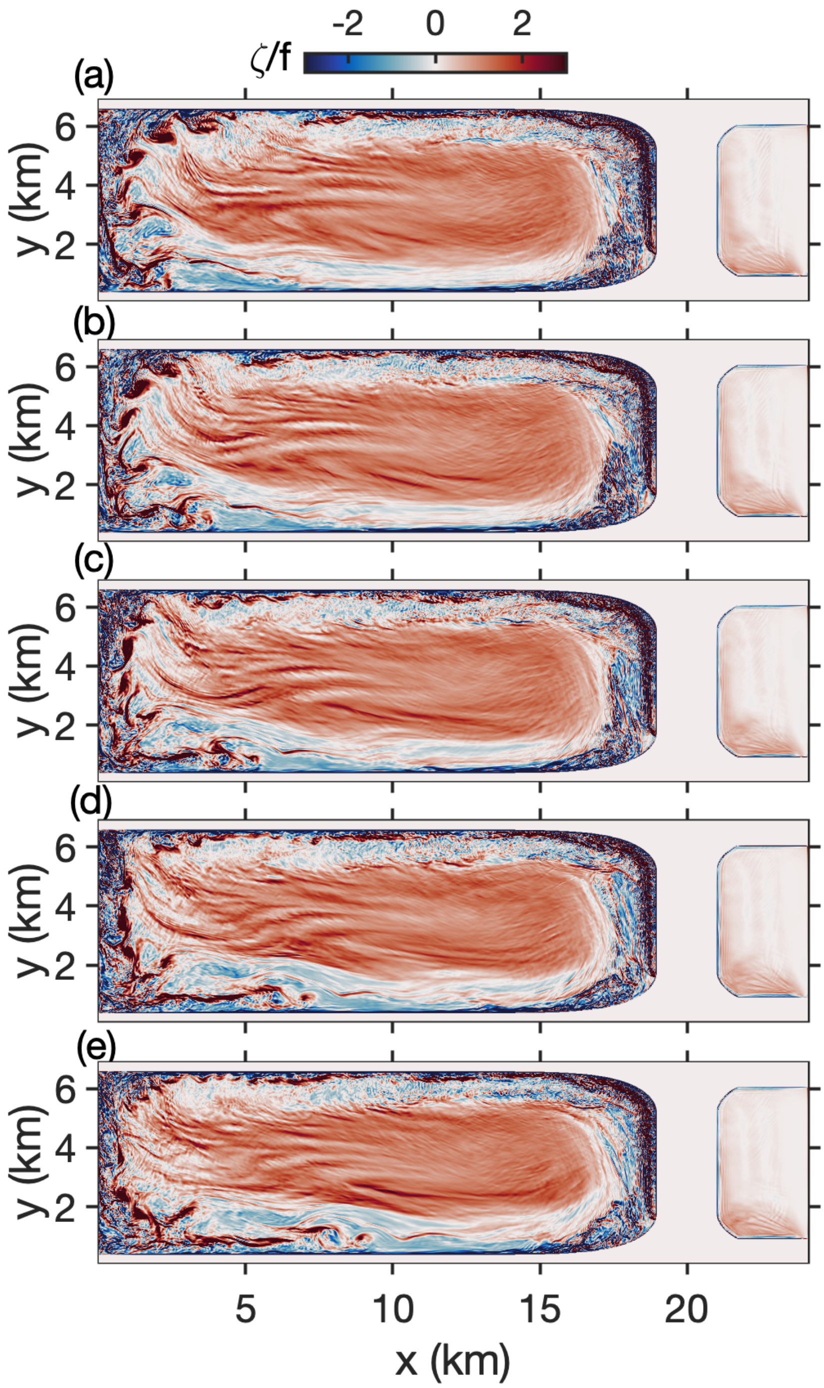

Figure S1. Snapshots of normalized vorticity of the reference simulation at $z = -320$ m at time (a) 90.0, (b) 90.1, (c) 90.2, (d) 90.3, (e) 90.4 days, showing a sequence of eddies being shed into the interior horizontal recirculation.

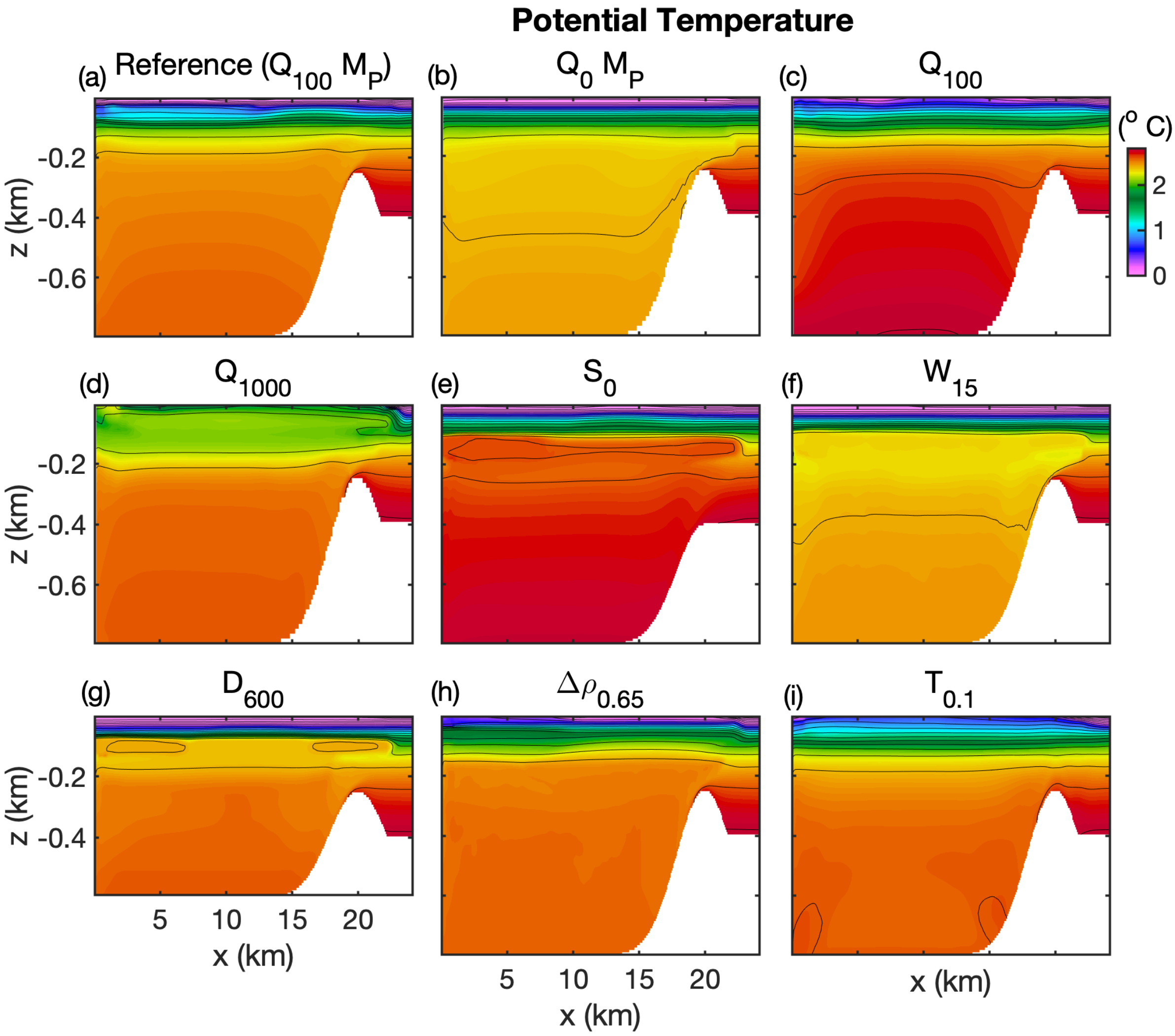

Figure S2. (a)-(i) Time- and meridionally-averaged potential temperature profiles for 9 experiments with varying parameters (see Table S1 for specific parameters for each case). The contour spacing is 0.2 °C.

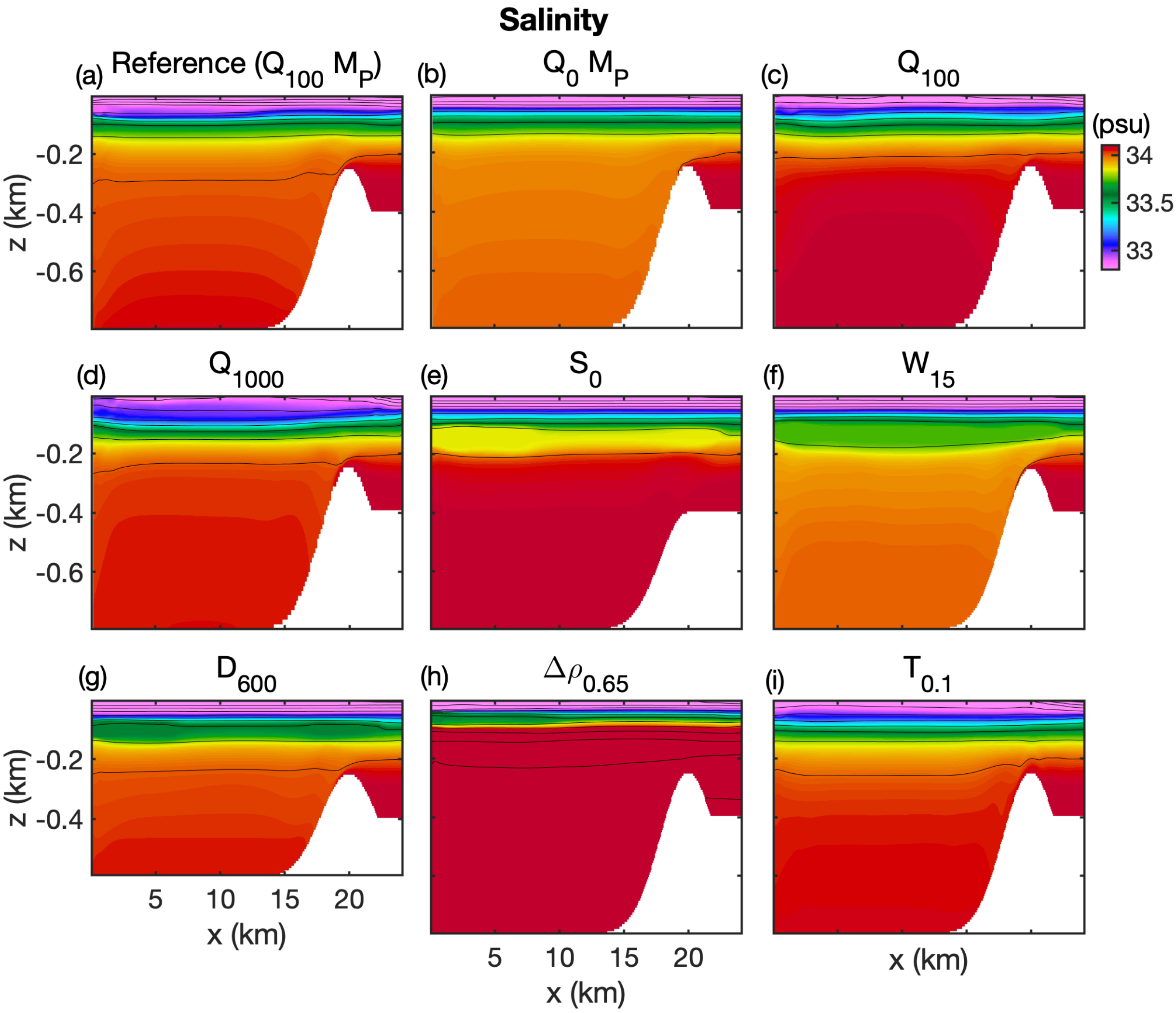

Figure S3. (a)-(i) Time- and meridionally-averaged salinity profiles for 9 experiments with varying parameters (see Table S1 for specific parameters for each case). The contour spacing is 0.2 psu.

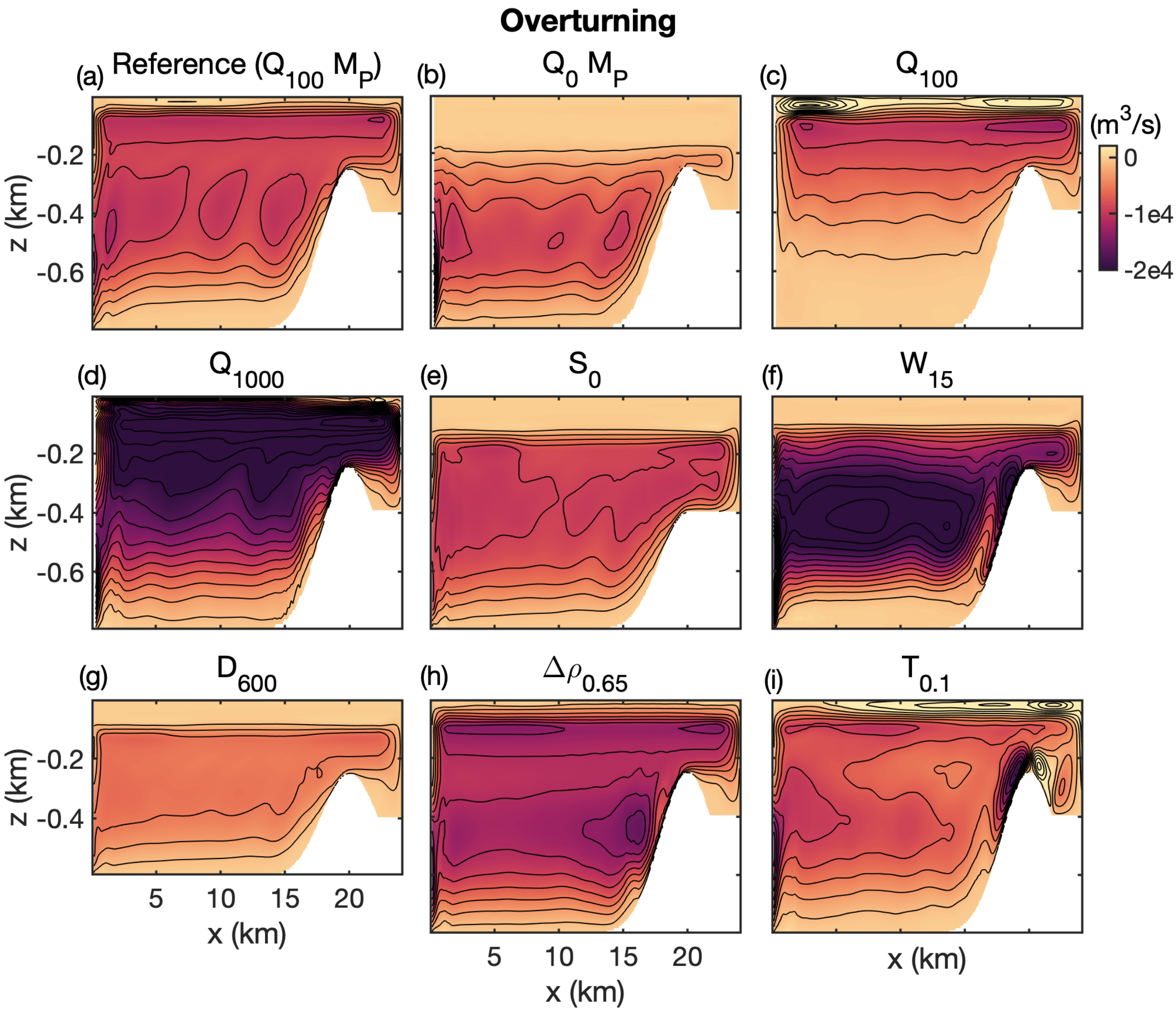

Figure S4. (a)-(i) Time-averaged overturning circulation for 9 experiments with varying parameters (see Table S1 for specific parameters for each case). The contour spacing is 2×10^3 m^3/s.

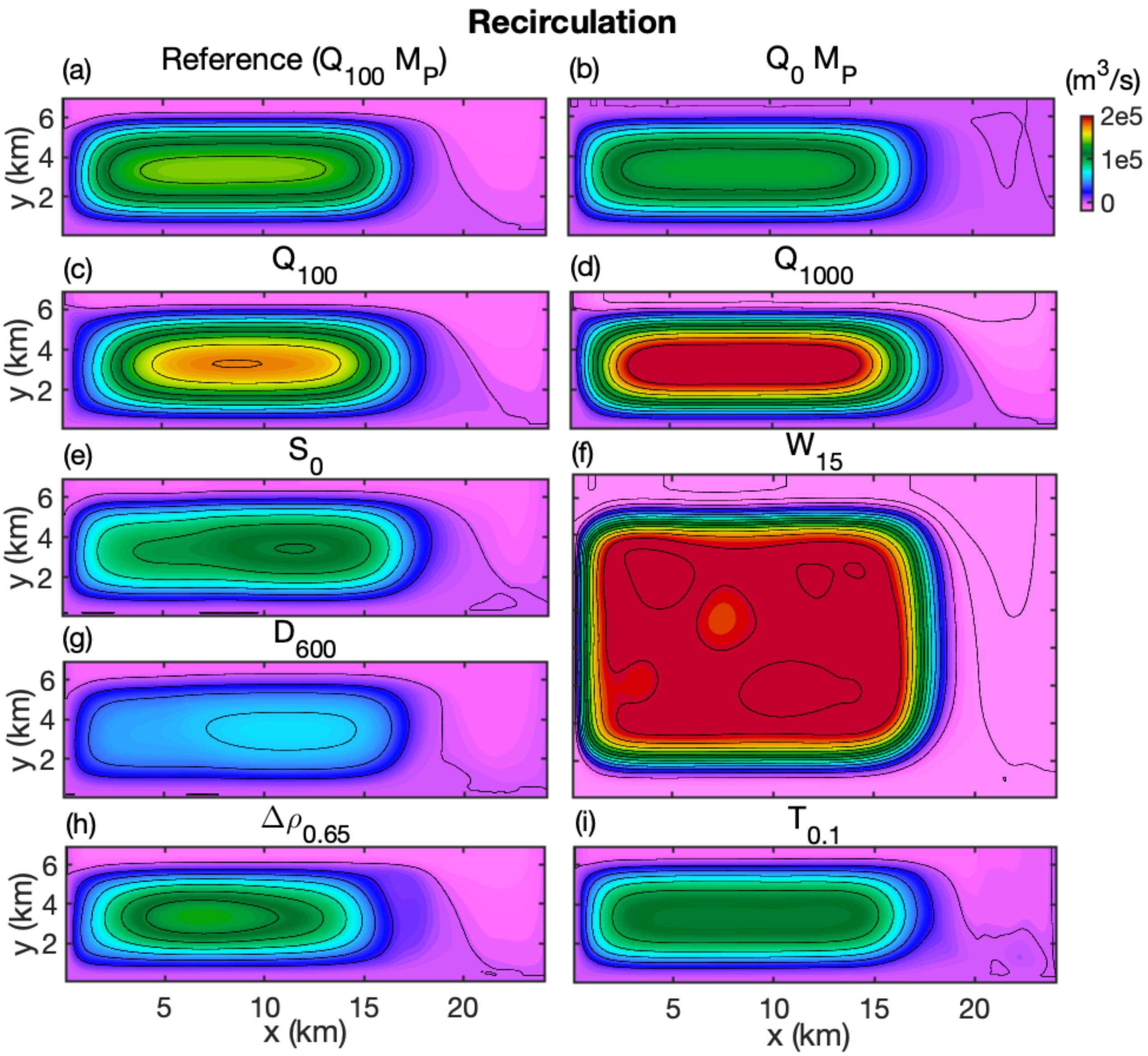

Figure S5. (a)-(i) Time-averaged horizontal recirculation integrated over depth (excluding circulation above the neutral buoyancy depth) for 9 experiments with varying parameters (see Table S1 for specific parameters for each case). The contour spacing is 2×10^4 m^3/s.

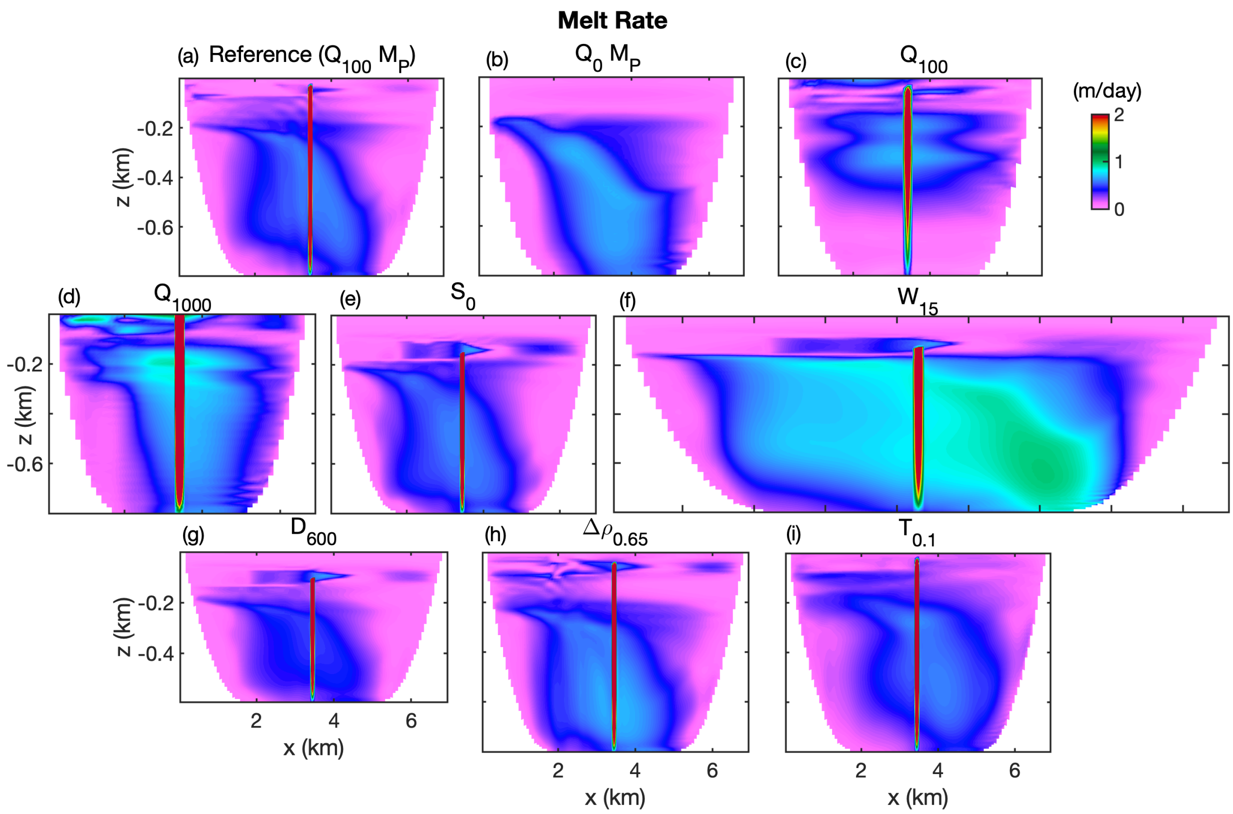

Figure S6. (a)-(i) Time-averaged melt rates (m/day) at the glacial face for 9 experiments with varying parameters (see Table S1 for specific parameters for each case).

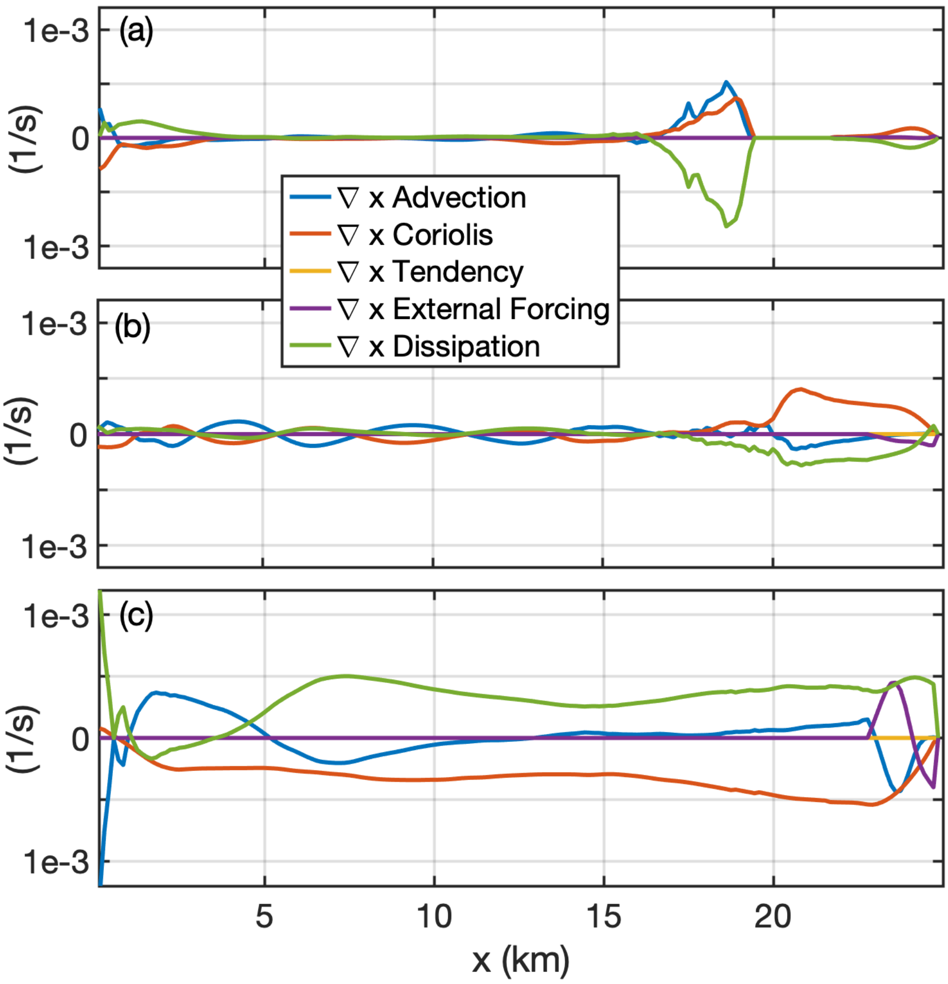

Figure S7. Vorticity balance in our reference experiment showing the depth-integrated meridionally-integrated curl of the momentum equation terms, cumulatively-integrated w.r.t. x starting from $x = 0$ in (a) the top 200 m, (b) -400 m $< z < -200$ m, and (c) the bottom 400 m. See Zhao et al. (2021) for a derivation of the terms used in the vorticity balance.

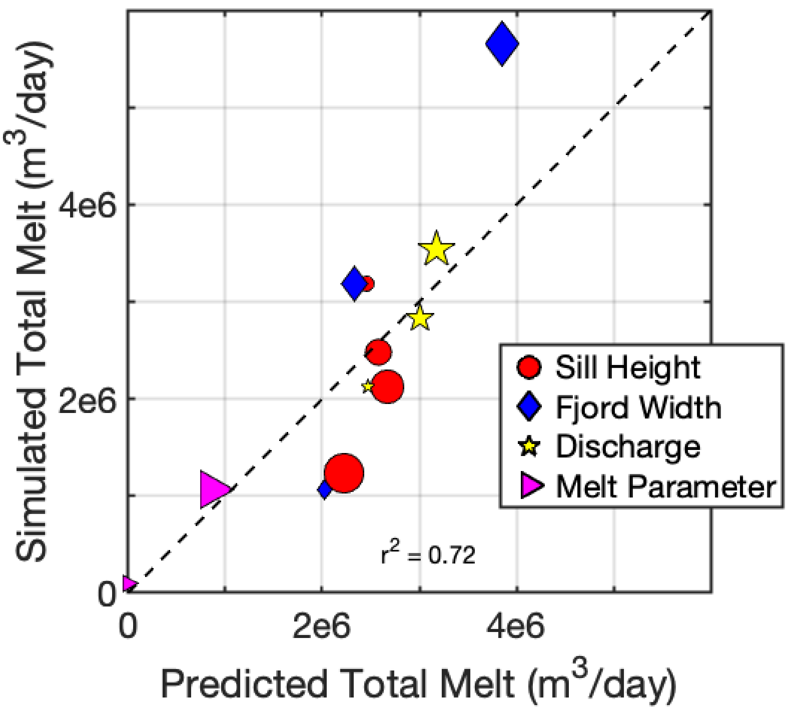

Figure S8. Simulation-diagnosed vs. theoretical predictions for the overall glacial melt rate based on the overturning and recirculation theory (Eqs. (11) and (10)).